INTERNATIONAL JOURNAL FOR NUMERICAL METHODS IN FLUIDS, VOL. 24, 645–670 (1997)

AN ADAPTIVE FINITE ELEMENT SCHEME FOR HYDRAULIC FRACTURING WITH PROPPANT TRANSPORT

S. OUYANG, G. F. CAREY AND C. H. YEW

Engineering Mechanics, University of Texas at Austin, Austin, Texas 78712, U.S.A.

SUMMARY

A mathematical model and adaptive finite element scheme are developed for describing the distribution of proppant in a propagating hydraulic fracture. The governing equation for proppant concentration is derived by applying the conservation law of mass to the proppant and to the proppant-laden fluid. Shah's empirical equation, which relates the proppant concentration and the indices of the non-Newtonian fluid, is used to describe the proppant-laden fluid. The proppant distribution inside a hydraulic fracture can then be obtained by solving the proppant concentration equation together with the governing equations of fluid and elasticity for a hydraulic fracturing. A novel moving grid scheme is developed that combines grid point insertion with redistribution. Four examples corresponding to different *in situ* stress distributions are computed to demonstrate the scheme. © 1997 by John Wiley & Sons, Ltd.

KEY WORDS: hydraulic fracturing; finite elements; moving adaptive grids

1. INTRODUCTION

Hydraulic fracturing of reservoirs has been employed to enhance oil and gas production for more than 40 years. In a typical 'process' a frac-fluid slurry composed of a mixture of a fluid and proppant such as coarse sand is pumped at high pressure into a selected section of the well-bore. The fluid pressure generates a fracture extending into the rock medium. The width of the hydraulic fracture is maintained by the proppant transported into the fracture by the frac-fluid. This method has proved to be an effective and economical method for stimulating production from a declining reservoir. Since the fracturing process is conducted at a great depth, the minimum compressive stress in the rock medium is in the horizontal direction and the hydraulically induced fracture is a vertical fracture (Figure 1). It has also been established experimentally that the height of the hydraulic fracture is controlled largely by the vertical distribution of the minimum *in situ* stresses.

The propagation characteristics of a hydraulically induced fracture are important in designing a fracturing process. Knowing the reservoir rock properties, *in situ* stress distribution and frac-fluid properties, an accurate prediction regarding the opening width and shape of the fracture is sought for a given pumping rate and time. The first true 3D fracture model was developed by Clifton and Abou-Sayed.[1,2] More recently this model has been extended to include multiple fluids, proppant transport and thermal effects as well as layered formations with different elastic moduli by Clifton and Wang.[3] Other 3D fracture models or codes based on the same field equations but different solution methodologies were developed by Cleary *et al.*[4] and Gu and Yew.[5] The model developed by Gu and Yew has a superior approach to the fracture problem but does not include the analysis and effects of

CCC 0271–2091/97/070645–26 $17.50

Received 17 February 1995
Revised 10 January 1996

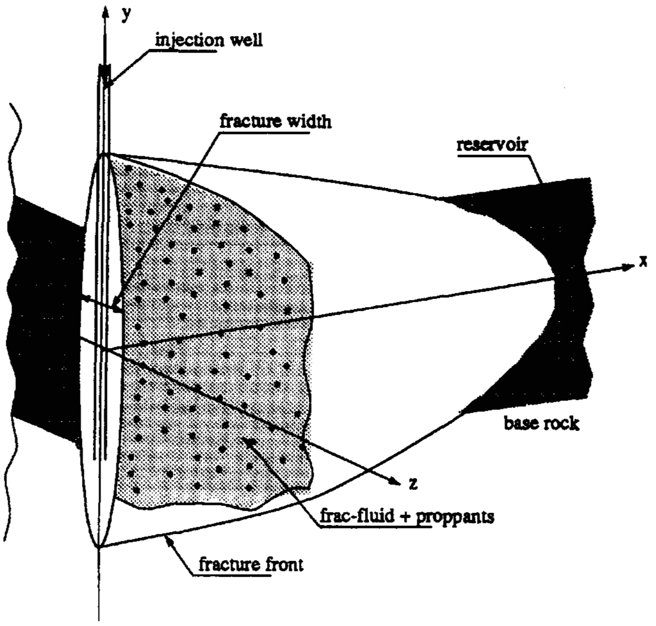

Figure 1. Configuration of a hydraulic fracture (not to scale)

proppant transport inside the hydraulic fracture. The present research addresses this problem and extends their approach to include finite element analysis of coupled proppant transport with fracture analysis. It also addresses the need for improved grid strategies, since the simulation of this type of problem is known to break down because of excessive grid deformation during fracture growth.

The present treatment is organized in the following manner. The governing equations for the propagation of a hydraulic fracture and the solution methodology in the GY-4M model of Gu and Yew[5] are briefly summarized in Section 2. Next the governing equation for the proppant concentration inside a hydraulic fracture is derived in Section 4 by applying the law of conservation of mass to the slurry and Fick's law of mass diffusion for a binary system. Shah's empirical equations are then employed to relate the corresponding alteration of the rheological properties of the slurry. Knowing the rheological properties of the slurry flow, the fluid pressure and fracture opening width as well as the propagation of a hydraulic fracture can be computed from the governing equations. The development of the proppant concentration equation and the implementation of this equation in the solution algorithm are presented. Some programming and computational aspects are given in Section 5 and numerical results for several important and representative test cases follow in Section 6.

2. FRAC-FLUID EQUATIONS

In the following derivations the frac-fluid slurry is assumed to be an incompressible non-Newtonian fluid, with the apparent viscosity η of the fluid described by a power-law model[6] as

$$\eta([D]) = k[2\mathrm{tr}([D]^2)]^{(n-1)/2}, \tag{1}$$

where $[D]$ is the rate-of-strain tensor for fluid velocity $\mathbf{v}$, n is the power-law index and k is the consistency coefficient of the fluid. Later we define how k and n depend on the proppant concentration c in the slurry.

In a hydraulic fracture the slurry flows inside a large but narrow opening with the ratio of length to width of the order of 10^4 or higher. Owing to the narrowness of the fracture opening, the fluid pressure variation across the fracture width (z-direction) is negligible and the derivatives of the fluid velocity components in the x–y plane with respect to z are much larger than are the other derivatives of the velocity components. Taking the assumption of narrow fracture opening width into consideration, the continuity equation of the slurry can be written for the two-dimensional fracture section Ω as

$$\frac{\partial}{\partial t}(\rho w)+\frac{\partial(\rho v_x w)}{\partial x}+\frac{\partial(\rho v_y w)}{\partial y}=-q_1\rho_f \tag{2}$$

or

$$\frac{\partial}{\partial t}(\rho w)+\nabla\cdot(\mathbf{v}w\rho)=-q_1\rho_f, \tag{3}$$

where ρ is the density of the slurry, ρ_f is the density of the fluid, w is the fracture width and v_x and v_y are the velocity components in the x- and y-direction respectively. The term $q_1\rho_f$ on the right-hand side of the above equations is the mass flow rate of fluid that leaks through the porous fracture surface into the rock formation. The leak-off volume rate per unit fracture area may be modelled by an empirical formula $q_1=2c_1/\sqrt{[t-\tau(x,y)]}$, where c_1 is the leak-off coefficient which is to be determined experimentally, $\tau(x,y)$ is the time at which the fluid starts to leak off at position (x,y) and t is the current pumping time.

It can be shown,[7] by considering the linear momentum equation and neglecting the sedimentation of proppants, that for a power-law fluid the flow rates are related to the pressure gradient by

$$wv_x=-\frac{n}{2n+1}k^{-1/n}\left[\left(\frac{\partial p}{\partial x}\right)^2+\left(\frac{\partial p}{\partial y}\right)^2\right]^{-(n-1)/2n}\frac{w^{(2n+1)/n}}{2^{(n+1)/n}}\frac{\partial p}{\partial x}. \tag{4}$$

$$wv_y=-\frac{n}{2n+1}k^{-1/n}\left[\left(\frac{\partial p}{\partial x}\right)^2+\left(\frac{\partial p}{\partial y}\right)^2\right]^{-(n-1)/2n}\frac{w^{(2n+1)/n}}{2^{(n+1)/n}}\frac{\partial p}{\partial y}. \tag{5}$$

Substituting equations (4) and (5) into equation (2) gives the following governing equation for the frac-fluid:

$$\begin{aligned}&\frac{\partial}{\partial x}\left\{\frac{n}{2n+1}k^{-1/n}\frac{w^{(2n+1)/n}}{2^{(n+1)/n}}\left[\left(\frac{\partial p}{\partial x}\right)^2+\left(\frac{\partial p}{\partial y}\right)^2\right]^{-(n-1)/2n}\frac{\partial p}{\partial x}\rho\right\}\\&+\frac{\partial}{\partial y}\left\{\frac{n}{2n+1}k^{-1/n}\frac{w^{(2n+1)/n}}{2^{(n+1)/n}}\left[\left(\frac{\partial p}{\partial x}\right)^2+\left(\frac{\partial p}{\partial y}\right)^2\right]^{-(n-1)/2n}\frac{\partial p}{\partial y}\rho\right\}=\frac{\partial}{\partial t}(w\rho)+q_1\rho_f.\end{aligned} \tag{6}$$

Next let us consider the corresponding boundary conditions. The boundary of the flow domain can be divided into three portions, $\partial\Omega=\partial\Omega_p\cup\partial\Omega_c\cup\partial\Omega_f$, as shown in Figure 2. The vertical section $\partial\Omega_p$ is along the perforated region $-y_p\leqslant y\leqslant y_p$, $x=0$ through which the frac-fluid and proppants are pumped into the fracture. The flow condition here can be written as

$$-\frac{nk^{-1/n}}{2n+1}\left[\left(\frac{\partial p}{\partial x}\right)^2+\left(\frac{\partial p}{\partial y}\right)^2\right]^{-(n-1)/2n}\frac{w^{(2n+1)/n}}{2^{(n+1)/n}}\frac{\partial p}{\partial n}\rho=-q_o\rho_o \quad \text{on} \quad \partial\Omega_p, \tag{7}$$

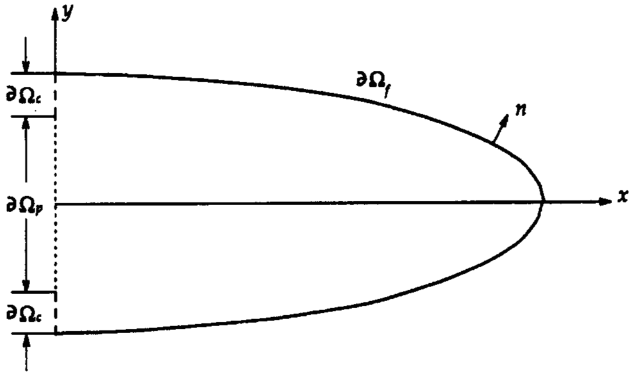

Figure 2. Illustration of boundary of flow domain

where q_0 is the given pumping rate of the mixture of frac-fluid and proppants (slurry) per unit length of the perforated region and ρ_0 is the density of the slurry in the perforated region. The remainder of the vertical symmetry section is denoted $\partial\Omega_c$ and from symmetry the flow here is zero. The flow rate normal to the fracture front $\partial\Omega_f$ is also zero. This implies

$$-\frac{nk^{-1/n}}{2n+1}\left[\left(\frac{\partial p}{\partial x}\right)^2+\left(\frac{\partial p}{\partial y}\right)^2\right]^{-(n-1)/2n}\frac{w^{(2n+1)/n}}{2^{(n+1)/n}}\frac{\partial p}{\partial n}\rho=0 \quad \text{on} \quad \partial\Omega_c \quad \text{and} \quad \partial\Omega_f. \tag{8}$$

Following Bui,[8] the equation which relates the surface traction and fracture opening displacement may be written as

$$-p(x,y)+\sigma(x,y)=\frac{G}{4\pi(1-\nu)}\int_\Omega\left[\frac{\partial}{\partial x}\left(\frac{1}{r}\right)\frac{\partial w}{\partial x'}+\frac{\partial}{\partial y}\left(\frac{1}{r}\right)\frac{\partial w}{\partial y'}\right]\mathrm{d}x'\mathrm{d}y'. \tag{9}$$

where r is the distance between the source point (x', y') and a field point (x, y), $\sigma(x, y)$ is the *in situ* stress and G and ν are the shear modulus and Poisson ratio respectively of the rock medium. Note that in view of the fracture assumptions the fracture surface may be taken as planar and hence the flow domain and fracture surfaces are both taken as Ω. The boundary condition for the above equation is that the fracture opening width is zero along the fracture front, i.e. $w(x, y, t) = 0$ on $\partial\Omega_f$.

Equations (6) and (9) can be solved numerically for $p(x, y)$ and $w(x, y)$ by applying the finite element method.

2.1. Finite element formulation

The planar fracture surface is discretized by a strip of quadrilateral singular elements along the fracture front (to model the stress singularity at the fracture tip), with triangular elements in the remainder of the mesh. The pressure p and fracture opening width w are approximated by

$$p(x,y)=\sum_{i=1}^{N}\phi_i(x,y)p_i, \qquad w(x,y,t)=\sum_{i=1}^{N}\phi_i(x,y)w_i(t). \tag{10}$$

where $\{\phi_i\}$ are the basis functions and $\{p_i\}$ and $\{w_i\}$ are the nodal values of the approximate solution for the fluid pressure and the fracture opening width at nodal point i respectively.

The weak integral forms of equations (6) and (9) are then discretized, leading to the coupled systems

$$[K_\mathrm{w}]\{w\} = \{f_\mathrm{t}\}, \tag{11}$$

$$[K_\mathrm{p}]\{p\} = -\{f_\mathrm{l}\} - \{f_\mathrm{w}\} + \{f_\mathrm{q}\}, \tag{12}$$

where

$$K_{\mathrm{p}ij} = \int_\Omega \frac{nk^{-1/n}}{2n+1}\frac{w^{(2n+1)/n}}{2^{(n+1)/n}}\left[\left(\frac{\partial p}{\partial x}\right)^2 + \left(\frac{\partial p}{\partial y}\right)^2\right]^{-(n-1)/2n}\left(\frac{\partial\phi_i}{\partial x}\frac{\partial\phi_j}{\partial x} + \frac{\partial\phi_i}{\partial y}\frac{\partial\phi_j}{\partial y}\right)\rho\mathrm{d}x\mathrm{d}y, \tag{13}$$

$$K_{\mathrm{w}ij} = \frac{G}{4\pi(1-\nu)}\int_\Omega\int_\Omega \frac{1}{r}\left(\frac{\partial\phi_i}{\partial x}\frac{\partial\phi_j}{\partial x'} + \frac{\partial\phi_i}{\partial y}\frac{\partial\phi_j}{\partial y'}\right)\mathrm{d}x'\mathrm{d}y'\mathrm{d}x\mathrm{d}y, \tag{14}$$

$$f_{\mathrm{l}i} = \int_\Omega \frac{2c_\mathrm{l}}{\sqrt{(t-\tau)}}\phi_i\rho_\mathrm{f}\mathrm{d}x\mathrm{d}y, \qquad f_{\mathrm{w}i} = \int_\Omega \frac{\partial w}{\partial t}\rho\phi_i\mathrm{d}x\mathrm{d}y, \qquad f_{\mathrm{q}i} = \int_{\partial\Omega} q_\mathrm{o}\rho\phi_i\mathrm{d}s, \tag{15}$$

$$f_{\mathrm{t}i} = \int_\Omega [p(x,y) - \sigma(x,y)]\phi_i(x,y)\mathrm{d}x\mathrm{d}y. \tag{16}$$

Natural boundary conditions apply on the boundary of the domain for the fluid equation (6). Moreover, the mass of slurry pumped into the fracture must equal the sum of the mass leaked off through the surface and the mass inside the fracture, i.e.

$$\int_{\partial\Omega_\mathrm{p}} q_\mathrm{o}\rho_\mathrm{o}\mathrm{d}s = \int_\Omega q_\mathrm{l}\rho_\mathrm{f}\mathrm{d}x\mathrm{d}y + \int_\Omega \frac{\partial w}{\partial t}\rho\mathrm{d}x\mathrm{d}y. \tag{17}$$

The time derivative $\partial w/\partial t$ in equations (15) and (17) can be approximated by a backward finite difference method as

$$\left.\frac{\partial w}{\partial t}\right|_m = \frac{w^{(m)} - w^{(m-1)}}{\Delta t}, \tag{18}$$

where $w^{(m)}$ and $w^{(m-1)}$ are the fracture opening widths at time steps t_m and t_{m-1} respectively.

On discretizing (17), this compatibility condition leads to a relation for time step Δt of the form

$$-\sum_i f_{\mathrm{l}i}^{(m)} - \frac{1}{\Delta t}\left(\sum_i f_{\mathrm{w}i}^{(m)} - \sum_i f_{\mathrm{w}i}^{(m-1)}\right) + \sum_i f_{\mathrm{q}i}^{(m)} = 0, \tag{19}$$

where index m is the time step. Hence the time increment Δt is determined simultaneously with the unknowns p and w.

Equations (11) and (12) which govern the hydraulic fracturing process are non- linear, time-dependent and involve a moving boundary. A quasi-steady process is assumed. Consider the fracture at time t_{m-1}. Let the location of the fracture front be denoted as $\partial\Omega^{m-1}$ and the fracture opening width $w^{(m-1)}$. During the next time step Δt the frac-fluid continues to be pumped into the fracture, causing an increase in the fluid pressure, in the fracture width and in the stress intensity factor at the fracture front. When the stress intensity factor exceeds the fracture toughness, the fracture front advances.

Solution proceeds by iteration until a convergent fracture width is obtained according to

$$\frac{\sum_i |w_{l+1}^{(m)} - w_l^{(m)}|_i}{\sum_i |w_{l+1}^{(m)}|_i} < \varepsilon, \tag{20}$$

where ε is the tolerance and l is the iteration index. In the present work the value of ε was taken as 10^{-6}.

The incremental distance Δd swept by the moving fracture front in a given time increment is related to the calculated stress intensity factor K_{I} and the critical stress intensity factor K_{IC} of the rock medium by the equation[9]

$$\Delta d = C\left(\frac{K_{\mathrm{I}} - K_{\mathrm{IC}}}{K_{\mathrm{IC}} + \sigma H/\sqrt{h}}\right)^{\gamma} \quad \text{for} \quad K_{\mathrm{I}} > K_{\mathrm{IC}}, \tag{21}$$

where σ is the local *in situ* stress at the fracture front, H is the local fracture height, h is the depth of fracture in the high *in situ* stress layer and C and γ are material constants. Here the advancement of the fracture front is controlled by the *in situ* stress σ and by the depth h of the fracture in the high-stress zone.

3. ADAPTIVE REMESHING

The major difficulty in hydraulic fracture problems is that the size of the final domain is much larger (say 10 or more times larger after some 30 min of injection) than that of the initial domain and the configuration of the domain will be significantly changed as the fracture propagates. An automatic and domain-adaptive remeshing scheme for studying the propagation of hydraulic fractures is presented next. The techniques of smoothing and Delaunay triangulation are employed to ensure the regularity of elements and the smoothness of the mesh. In addition, a scheme for adding new nodal points (and consequently new elements) to refine the mesh is used when the fracture domain is highly contained or significantly changed in size.

First the nodes on the fracture tip are moved to the new fracture tip position. Based on the set of nodal points generated on the fracture front, we can easily create a corresponding set to define a narrow strip of quadrilateral elements. These points on the strip of quadrilaterals also serve as the boundary points of the inner region to be triangulated. Before retriangulation, however, points in the interior are 'convected' proportionally with the advancing fracture tip by taking a weighted average of the co-ordinates with those of the surrounding nodes (in a manner similar to a Gauss–Seidel update). Hence nodes near the fracture tip have proportionally higher convection than those far away from the tip.

As the fracture advances, the domain and fracture boundary increase in size. New nodal points are inserted on the fracture surface as follows. Let the node spacing h_i be defined as the distance between two adjacent nodes i and $i+1$ on $\partial\Omega_{\mathrm{f}}$. Let $h_{\min}$ be the minimum node space along the boundary. The criterion for front refinement is $h_i/h_{\min} > \beta$, where β is a specified parameter to control the spacing.

Following the insertion of new nodes on the boundary, the ratio between the adjacent node spacings, defined as

$$\rho_i = \frac{h_i}{h_{i-1}} \quad \text{for} \quad i = 1, 2, \ldots, N_{\mathrm{b}} - 1, \tag{22}$$

is checked to ensure the smoothness of the boundary node gradation. Two parameters, $\rho_{\min}$ and $\rho_{\max}$, are introduced to determine whether local smoothing is to be applied: if ρ_i is between $\rho_{\min}$ and $\rho_{\max}$, there is no need for smoothing; if $\rho_i > \rho_{\max}$, node i is moved proportionally towards node $i+1$ and vice versa.

As the domain grows, new nodes must also be added in the interior and then the domain remeshed. First, points are inserted and repositioned on the boundary as indicated above. Next, new nodes are inserted at the centroid of interior triangles that exceed a specified relative area ratio. The node point locations are locally smoothed based on adjacent node positions and angles. Finally a new Delaunay triangulation is constructed.

As an example, the remeshed grid for the propagation of a hydraulic fracture under the action of a uniform *in situ* stress distribution is shown in Figure 3(a). The elements in the remeshed grid have nearly the same size and the elements are distributed uniformly in the grid. The grid shown in Figure 3(a) also demonstrates the capability of the scheme to insert nodes on the boundary as well as inside the domain. After 30 min of pumping, the number of elements increases from the original 82 to 204.

Similarly, Figure 3(b) shows the final grid (after 30 min of pumping) for a hydraulic fracture under an *in situ* stress contrast of 50 psi. Comparing with the uniform *in situ* stress case, more boundary nodes are inserted, since the fracture is contained and the boundary of the domain is slightly elongated. As a consequence, one can expect the numerical results based on the remeshed grid to be more accurate than those from the old grid. In this case the number of elements increases from 82 to 202.

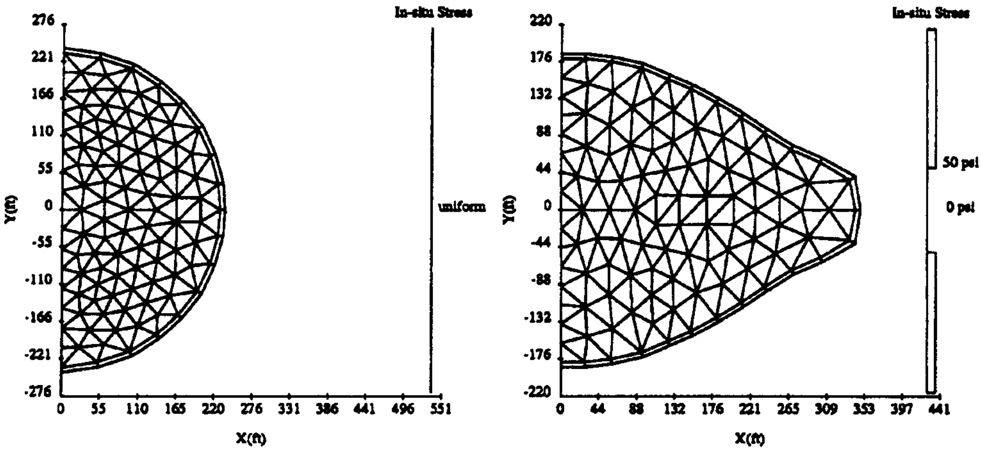

(a) Uniform In-situ Stress

(b) 50 *psi* In-situ Stress Contrast

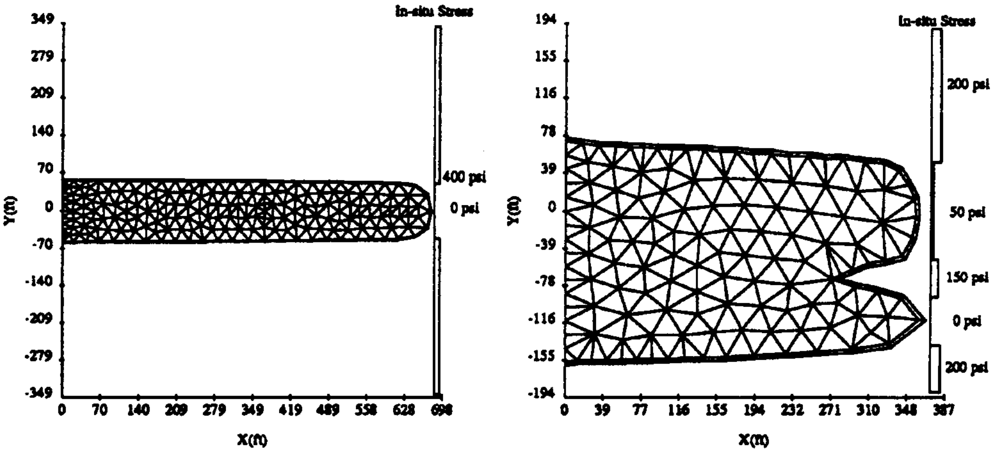

Figure 3. Final meshes after 30 min of pumping

Figure 3(c) shows the final grid for a hydraulic fracture under a high *in situ* stress contrast of 400 psi. By applying the present remeshing scheme, it is seen that again the elements are relatively uniformly distributed and there are no slender elements in the domain despite the elongation of the fracture. The accuracy of the computation is therefore maintained as the fracture propagates. The number of elements increases from 76 to 264 in this case.

Finally, under the action of a complex *in situ* stress distribution, we obtain the final mesh shown in Figure 3(d). Again the elements are uniformly distributed in the domain and there is no element overlap in the kinked region. In this case the number of elements increases from 82 to 262.

In each of the above cases the computation breaks down in the absence of point insertion, smoothing and Delaunay triangulation. In the fourth case, for example, the computation fails very early in the simulation owing to element overlap near the concave region resulting from the complex *in situ* stress contrast.

4. PROPPANT TRANSPORT

In hydraulic fracturing operations the fracture is first initiated with a fluid of low viscosity and then followed by fluids (or gels) containing proppants. The use of a low-viscosity fluid in the initial phase of fracturing is to reduce the friction loss during the fracturing process. The proppant- laden fluid is later introduced into the fracture to maintain the fracture opening width during and after the fracturing operation.

Let the volume concentration of the proppant, $c(x, y, t)$, be defined as the volume of proppant per unit volume of slurry (fluid + proppant): $c(x, y, t) = V_p/V$, where V_p is the volume of proppant in slurry volume V. Similarly, let ρ_{ps} be the total mass of proppant per unit volume of slurry. Then, by definition,

$$\rho_{ps} = \frac{M_p}{V} = \frac{V_p}{V}\frac{M_p}{V_p} = c\rho_p. \tag{23}$$

Let $w(x, y, t)$ be the fracture opening width and let wq_{px} and wq_{py} be the x- and y-components of the mass flux vector $w\mathbf{q}_p$ for the proppant. Mass conservation of proppant then implies

$$\frac{\partial}{\partial t}(\rho_{ps}w) + \nabla \cdot (\mathbf{q}_p w) = 0. \tag{24}$$

The proppant flux $\mathbf{q}_p$ is the product of ρ_{ps} and the proppant component velocity $\mathbf{v}_p$, i.e. $\mathbf{q}_p = \rho_{ps}\mathbf{v}_p$. This velocity can be related to the bulk fluid velocity by introducing the diffusive proppant flux $\mathbf{J}_p$:[10]

$$\mathbf{q}_p = \rho_{ps}\mathbf{v} + \mathbf{J}_p. \tag{25}$$

In turn, $\mathbf{J}_p$ can be modelled by Fick's law as

$$\mathbf{J}_p = -\rho D_{pf}\nabla\omega_p, \tag{26}$$

where $\omega_p = \rho_{ps}/\rho$ is the mass fraction of proppant. Combining these relations, we obtain the governing equation for proppant transport in terms of the mass concentration:

$$\frac{\partial}{\partial t}(\rho_{ps}w) + \nabla \cdot (\rho_{ps}w\mathbf{v}) = \nabla \cdot (\rho w D_{pf}\nabla\omega_p). \tag{27}$$

In existing hydraulic fracture models the molecular diffusion is small and the fracture flow is taken as laminar at constant temperature. Hence the diffusivity in (27) is negligible. In applications it is more convenient to use the volume concentration c of the proppant in place of the mass concentration ρ_{ps}. Substituting (23) into (27), we then obtain

$$\frac{\partial}{\partial t}(c\rho_{\mathrm{p}}w) + \nabla \cdot (c\rho_{\mathrm{p}}w\mathbf{v}) = 0. \tag{28}$$

The mass of the slurry, ρV, is the sum of the mass of the proppant, $\rho_{\mathrm{p}}V_{\mathrm{p}}$, and the mass of the frac-fluid, $\rho_{\mathrm{f}}V_{\mathrm{f}}$, i.e. $\rho V = \rho_{\mathrm{f}}V_{\mathrm{f}} + \rho_{\mathrm{p}}V_{\mathrm{p}}$, where V_{f} is the volume of the frac-fluid. Notice that $V_{\mathrm{f}} = V - V_{\mathrm{p}}$ and $c = V_{\mathrm{p}}/V$, so $\rho = c\rho_{\mathrm{p}} + (1-c)\rho_{\mathrm{f}}$. Substituting these relations into the fluid equation (3),

$$\frac{\partial}{\partial t}\{[c\rho_{\mathrm{p}} + (1-c)\rho_{\mathrm{f}}]w\} + \nabla\cdot \{[c\rho_{\mathrm{p}} + (1-c)\rho_{\mathrm{f}}]w\mathbf{v}\} = -q_{\mathrm{l}}\rho_{\mathrm{f}}. \tag{29}$$

Subtracting equation (28) from equation (29) and observing that ρ_{f} is constant for an incompressible fluid, the concentration of proppant satisfies

$$w\frac{\partial c}{\partial t} + wv_x\frac{\partial c}{\partial x} + wv_y\frac{\partial c}{\partial y} - (1-c)\left(\frac{\partial w}{\partial t} + \frac{\partial(wv_x)}{\partial x} + \frac{\partial(wv_y)}{\partial y}\right) = q_{\mathrm{l}}. \tag{30}$$

The first term of the equation is the change in proppant concentration in the fracture with time. The second and third terms represent the change in proppant concentration by convection of the slurry flow. The fourth term involves the effect of the change in fracture opening width on the proppant concentration as the fracture propagates. The final term shows the effect of the leak-off of frac-fluid: the more the frac-fluid leaks, the higher is the concentration. The boundary conditions become $c = c_{\mathrm{p}}$ on $\partial\Omega_{\mathrm{p}}$ and $\partial c/\partial n = 0$ elsewhere. Initially, $c(x, y, 0) = 0$ in Ω. Physically, when the width is too small near the fracture front, the proppant cannot pass through to the fracture tip, so the concentration in this region is zero; that is, for a node i, if $w_i \leqslant d$, then $c_i = 0$, where d is the diameter of the proppant. This condition may be applied in the vicinity of the fracture front.

It is well-known that the rheological property of the fluid (or slurry) is altered by the presence of proppants. Here we make the usual assumption of power-law behaviour. The empirical relations of Shah[11] for power- law index n and consistency coefficient k introduced in the present work; that is, we set

$$n = A\mathrm{e}^{Bc}, \qquad k = P\mathrm{e}^{Qc}, \tag{31}$$

where A, B, P and Q are parameters which depend upon the properties of a particular fluid and the proppant and have to be determined by experimentation.

An extensive experimental study on the correlation for a particular fracturing slurry has been carried out by Shah.[11] Based on the experimental data, the corresponding values of constants A, B, P and Q can be determined by using a curve-fitting technique with the exponential model. These values are listed in Table I for different proppant concentrations and will be used in the numerical case studies later.

After solving for the proppant concentration distribution, the nodal values of the index n and the consistency coefficient k of the power-law model for the non-Newtonian fluid can be calculated and then applied to calculate the pressure p.

Table I. Parameters for power-law index n and consistency coefficient k (from Reference 11)

Temperature (°F)	HPG/MGAL	A	B	P	Q
80	30 LB	0·53	−2·29	0·0068	6·51
	40 LB	0·40	−3·43	0·0304	6·38
	60 LB	0·28	−4·21	0·1089	4·71
110	30 LB	0·56	−1·41	0·0050	6·45
	40 LB	0·48	−2·38	0·0161	6·60
	60 LB	0·39	−3·33	0·0659	5·58
140	30 LB	0·58	−1·26	0·0038	6·58
	40 LB	0·51	−2·32	0·0095	6·98
	60 LB	0·40	−3·42	0·0497	6·01

4.1. *Finite element implementation*

A variational form for the proppant transport problem on a fixed domain can be constructed by introducing weighted residual projections for the governing partial differential equation (30):

$$\int_\Omega\left(w\frac{\partial c}{\partial t}-(1-c)\frac{\partial w}{\partial t}-\frac{\partial[(1-c)wv_x]}{\partial x}-\frac{\partial[(1-c)wv_y]}{\partial y}\right)q\,\mathrm{d}x\mathrm{d}y=\int_\Omega q_1q\,\mathrm{d}x\mathrm{d}y. \qquad (32)$$

Integrating (32) by parts and using the relations (4) and (5) for the velocity components, one obtains

$$\int_\Omega\left(\frac{\partial[(1-c)wv_xq]}{\partial x}+\frac{\partial[(1-c)wv_yq]}{\partial y}\right)\mathrm{d}x\mathrm{d}y$$
$$=\int_{\partial\Omega}-(1-c)q\frac{n}{2n+1}k^{-1/n}\left[\left(\frac{\partial p}{\partial x}\right)^2+\left(\frac{\partial p}{\partial y}\right)^2\right]^{-(n-1)/2n}\frac{w^{(2n+1)/n}}{2^{(n+1)/n}}\frac{\partial p}{\partial n}\mathrm{d}s. \qquad (33)$$

On the boundary sections $\partial\Omega_\mathrm{f}$ and $\partial\Omega_\mathrm{c}$, $\partial p/\partial n=0$. The weak statement of the proppant concentration equation becomes: find c satisfying $c=c_\mathrm{p}$ on $\partial\Omega_\mathrm{p}$ and such that

$$\int_\Omega\left[wq\frac{\partial c}{\partial t}+\left((1-c)wv_x\frac{\partial q}{\partial x}+(1-c)wv_y\frac{\partial q}{\partial y}\right)-(1-c)q\frac{\partial w}{\partial t}\right]\mathrm{d}x\mathrm{d}y=\int_\Omega q_1q\,\mathrm{d}x\mathrm{d}y \qquad (34)$$

for all admissible test functions q with $q=0$ on $\partial\Omega_\mathrm{p}$. Note that wv_x and wv_y are defined in terms of pressure and fracture width by (4) and (5).

The concentration c is approximated by using piecewise polynomial finite element basis functions

$$c(x,y,t)=\sum_{j=1}^{N}c_j(t)\phi_j(x,y) \qquad (35)$$

and the test functions are taken as $\{\phi_i\}$.

Substituting into (34) and using (4) and (5), we obtain the semidiscrete system of ordinary differential equations for the concentration

$$\begin{aligned}\sum_{j=1}^{N}\Bigg[\!\!\Bigg[\int_{\Omega}\Bigg\{&w\phi_i\frac{\mathrm{d}c_j}{\mathrm{d}t}\phi_j+\frac{n}{2n+1}k^{-1/n}\left[\left(\frac{\partial p}{\partial x}\right)^2+\left(\frac{\partial p}{\partial y}\right)^2\right]^{-(n-1)/2n}\frac{w^{(2n+1)/n}}{2^{(n+1)/n}}\\&\times\left(\frac{\partial p}{\partial x}\frac{\partial\phi_i}{\partial x}+\frac{\partial p}{\partial y}\frac{\partial\phi_i}{\partial y}\right)\phi_jc_j+\frac{\partial w}{\partial t}\phi_i\phi_jc_j\Bigg\}\mathrm{d}x\mathrm{d}y\Bigg]\!\!\Bigg]\\=\int_{\Omega}\Bigg\{&\left(q_1+\frac{\partial w}{\partial t}\right)\phi_i+\frac{n}{2n+1}k^{-1/n}\left[\left(\frac{\partial p}{\partial x}\right)^2+\left(\frac{\partial p}{\partial y}\right)^2\right]^{-(n-1)/2n}\frac{w^{(2n+1)/n}}{2^{(n+1)/n}}\\&\times\left(\frac{\partial p}{\partial x}\frac{\partial\phi_i}{\partial x}+\frac{\partial p}{\partial y}\frac{\partial\phi_i}{\partial y}\right)\Bigg\}\mathrm{d}x\mathrm{d}y,\quad i=1,2,\ldots,N,\end{aligned}\tag{36}$$

or, compactly in matrix form,

$$[A]\frac{\mathrm{d}\{c\}}{\mathrm{d}t}+[B]\{c\}=\{f_\mathrm{c}\}.\tag{37}$$

In the following computations a (dissipative) backward difference scheme is applied; that is, in each time step we solve

$$([A]^m+\Delta t[B]^m)\{c\}^m=[A]^m\{c\}^{m-1}+\Delta t\{f_\mathrm{c}\}^m,\tag{38}$$

where $[A]$ depends on the current solution w^m for the fracture width. The effect of including the pressure and fracture width relations explicitly in (36) is to stabilize the resulting Galerkin scheme as seen in the following numerical experiments.

5. COMPUTATIONAL ASPECTS

The solution for the pair w, p and the proppant concentration c is decoupled within each time step in the manner indicated by the algorithm in Figure 4.

5.1. *Performance studies*

In order to assess the efficiency of the implementation, the performance for the major subroutines in the code is checked and is summarized in Table II. These timing statistics are for the Sun Sparc Workstation (4-75) and indicate that about one-third of the CPU time is used for forming the fracture stiffness matrix $[K_\mathrm{w}]$ because of the calculation of the double integral in the fracture opening equation, while about one-fifth of the CPU time is spent forming the sparse fluid stiffness matrix $[K_\mathrm{p}]$; the Gaussian solver for the linear fracture and fluid systems is also a major CPU time consumer. Since $[K_\mathrm{w}]$ is a dense matrix and $[K_\mathrm{p}]$ is a sparse matrix, a regular Gaussian solver is employed for $[K_\mathrm{w}]$ whereas a banded solver is employed for $[K_\mathrm{p}]$. As expected, as the total number of nodes increases, the percentage of CPU time spent in the Gaussian solver grows non- linearly: the regular Gaussian solver has a time complexity of $O(n^3)$, where n is the number of nodes, and the banded Gaussian solver has a time complexity of $O(b_\mathrm{w}^2n)$, where b_w is the bandwidth. An iterative solution such as the biconjugate gradient method may also be applied for the pressure system. In fact, even for full systems such as the dense matrix problem in a boundary element formulation these Krylov space projectors may be faster than direct elimination, since the boundary element systems are frequently well- conditioned. By optimizing the node numbering, we may reduce the bandwidth b_w and improve

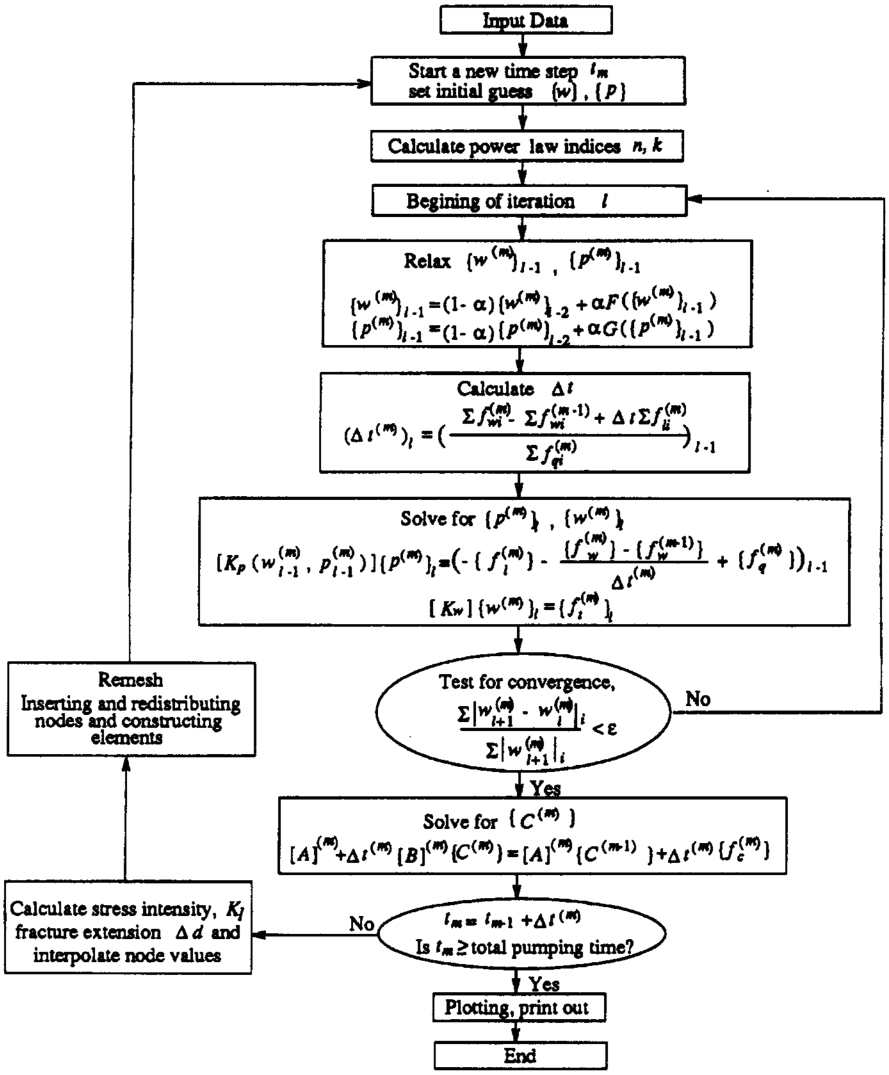

Figure 4. Flow chart of programme GYCO-PT

Table II. Timing statistics of code performance (%)

Number of nodes	Form K_w	Form K_p	K_w, K_p solver	Solve proppant	Remesh	Other
63	36·6	24·4	28·8	0·8	1·5	7·9
99	34·2	21·5	35·8	0·8	1·2	6·5
116	32·4	18·5	42·2	0·6	1·0	5·3

the performance of the Gaussian solver. The remesh scheme is very efficient and required only about 1 per cent of the CPU time. Finally, less than 1 per cent of the run time is spent solving the proppant concentration problem.

Owing to the nonlinearity, the fracture width w and fluid pressure p are adjusted by iteration within each time step. The following relaxation strategy is also applied within each iteration:

$$w_{l+1}^{(m)} = \alpha F(w_l^{(m)}) + (1-\alpha)w_l^{(m-1)}, \tag{39}$$

$$p_{l+1}^{(m)} = \alpha G(p_l^{(m)}) + (1-\alpha)p_l^{(m-1)}, \tag{40}$$

where α is the relaxation parameter. This method provides a linear extrapolation of the solution between the computed value and the value at the previous iterate level. In order to choose α as large as possible in the iteration process and still maintain convergence, an adaptive relaxation factor α_{ad} is used in the iteration process. If an increase in the sequence of $|\{w\}_{l+1}^{(m)} - \{w\}_l^{(m)}|$ occurs during the iteration process, we reduce the value of α proportionally. In order to obtain improved convergence, the starting value of α_{ad} is chosen based on the behaviour of the individual hydraulic fracture problem. For a 'smooth' hydraulic fracture problem (such as uniform or slight *in situ* stress contrast) a larger starting value of α can be set at the beginning of the iteration process, whereas for a 'tough' one (such as a complex or high *in situ* stress contrast) a relatively smaller starting value of α should be chosen. Generally speaking, for our hydraulic fracture problem a starting value of α between 0·2 and 0·3 is preferred at the beginning of the iteration process.

6. RESULTS

Since the behaviour of a hydraulically induced fracture and the associated proppant distribution are very sensitive to the *in situ* stress distribution, four different distributions of *in situ* stresses are considered. The formation properties, frac-fluid properties, fluid leak-off coefficient, initial fracture geometry and pumping schedule are the same for all the cases and are given in Table III. The *in situ* stress distributions and the corresponding parameters used for remeshing in each case are different and are also given in Table III.

6.1. *Uniform in situ stress*

The hydraulic fracture for a uniform *in situ* stress is expected to be a circular fracture. The final mesh is shown in Figure 5(a) and a sequence of fracture front contours in Figure 5(b). The variations in the net borehole pressure and maximum fracture opening width during the entire fluid injection period are shown in Figures 5(c) and 5(d) respectively. The existence of proppants in the fluid causes increases in the net borehole pressure and fracture width. Also, as the proppant concentration increases, the increments in the net borehole pressure and fracture width become large. These results are expected, as the fluid becomes more viscous when the concentration of proppant inside the fracture increases. The shape of the hydraulic fracture and distribution of proppants at $t = 11$, 12, 22, 28 and 30 min after the initial fluid injection are shown in Figures 6 and 7. Since the *in situ* stress distribution is uniform, the hydraulically induced fracture is circular as expected. The fluid is injected through a perforated length of 80 ft into the fracture. The proppant concentration is zero ($c = 0$) during the first 10 min of injection and the proppant concentration during the second stage of injection (10–20 min) is 3%. Consequently, the proppant concentration in a large region immediately behind the fracture front is zero and the concentration then increases slowly from zero to 3% in the

Table III. Input data

Formation and fluid properties and initial fracture geometry

Young modulus	10^6 psi	Perforated zone	80·0 ft
Poisson rato	0·3	Initial fracture length	20·0 ft
Fracture toughness	1000 lb $\mathrm{in}^{-3/2}$	Initial fracture height	100·0 ft
Leak-off coefficient	0·0005 ft $\mathrm{min}^{-1/2}$	$n = 0{\cdot}48\mathrm{e}^{-2{\cdot}38c}$,	
		$k = 0{\cdot}016\mathrm{e}^{6{\cdot}59c}$	

Pumping schedule

Stage no.	Pump time (min)	Injection rate (bubbles/min)	Fluid density (lb ft^{-3})	Proppant density (lb ft^{-3})	Proppant concentration (%)
1	0·0– 10·0	20·0	62·0	—	0·0
2	10·0– 20·0	20·0	62·0	150·0	3·0
3	20·0–26·0	20·0	62·0	150·0	5·0
4	26·0–30·0	20·0	62·0	150·0	10·0

In situ stress distribution

Case	Layer no.	y-Co-ordinate (ft)		Stress (psi) at interface	
		Lower	Upper	Lower	Upper
Uniform	1	−1000·0	1000·0	0·0	0·0
50 psi contrast	1	−1000·0	−50·0	50·0	50·0
	2	−50·0	50·0	0·0	0·0
	3	50·0	1000·0	50·0	50·0
400 psi contrast	1	−1000·0	−50·0	400·0	400·0
	2	−50·0	50·0	0·0	0·0
	3	50·0	1000·0	400·0	400·0
Complex contrast	1	−1000·0	−140·0	200·0	200·0
	2	−140·0	−90·0	0·0	0·0
	3	−90·0	−50·0	150·0	150·0
	4	−50·0	50·0	50·0	50·0
	5	50·0	1000·0	200·0	200·0

Parameters for remesh and iteration

	Uniform	50 psi contrast	400 psi contrast	Complex contrast
Maximum fracture tip movement (ft)	5·0	10·0	10·0	10·0
In situ stress in payzone (psi)	0·0	0·0	0·0	50·0
Relaxation factor (for iteration)	0·25	0·2	0·2	0·2
No. of nodes along borehole	15	15	9	15
β (for boundary node insertion)	1·52	1·8	2·0	1·9
θ (for boundary node smoothing)	10·0	12·0	9·0	10·0
q (for interior node insertion)	2·4	3·9	6·0	6·5

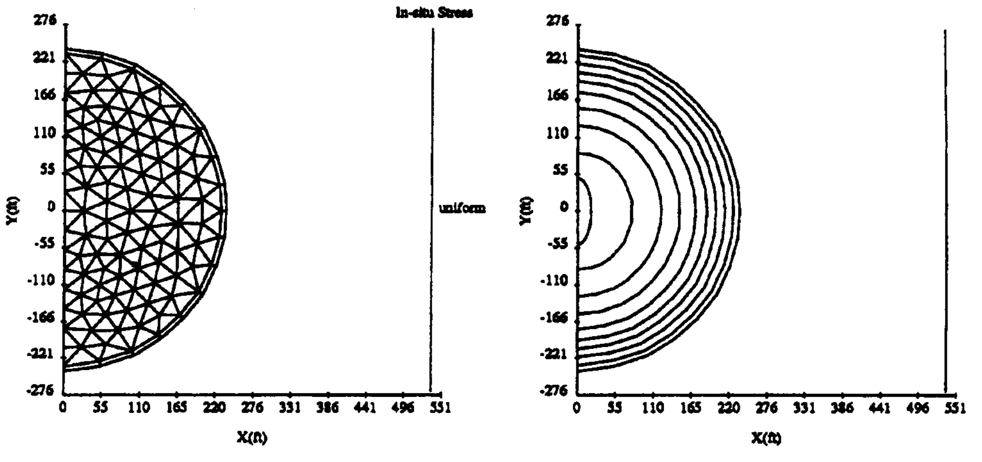

(a) Final Mesh (b) Fracture Front Contours at Different Times

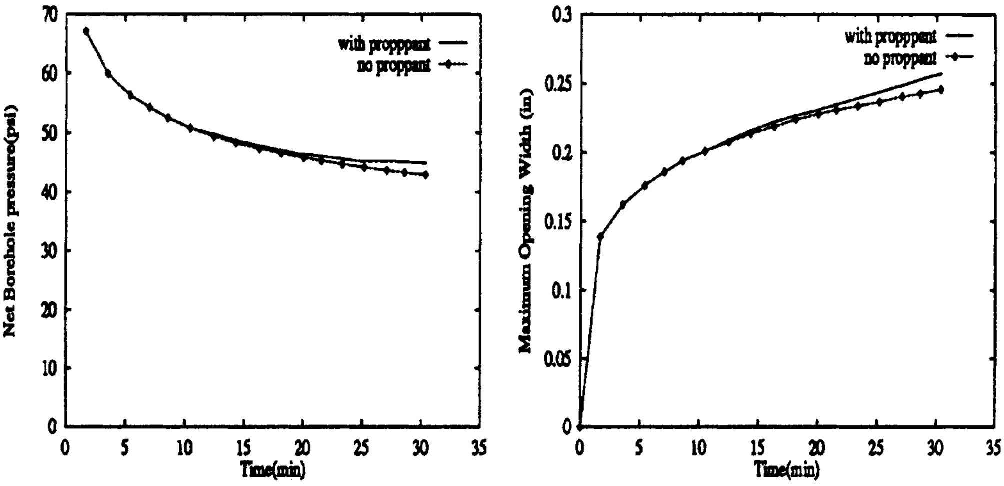

Figure 5. Results for uniform *in situ* stress

perforated region. The shape of proppant distribution inside the fracture is approximately elliptical, with a decrease in concentration from the entry region towards the fracture front region. The reduction of concentration due to convective flow of the frac-fluid is evident in Figure 6(b).

The proppant concentration 2 min after the third stage of fluid injection (with 5% proppant) is shown in Figure 6(c). The proppant concentration in the region near the perforation is 5 per cent and decreases to approximately 0·55% near the front. The final distribution of proppant concentration 4 min after the fourth stage of fluid injection ($c = 10\%$) is shown in Figure 7. The concentration of proppant in the region near the perforated zone is 10·6% and is approximately 1·1% in the region near the fracture tip. The concentration contours are almost circular.

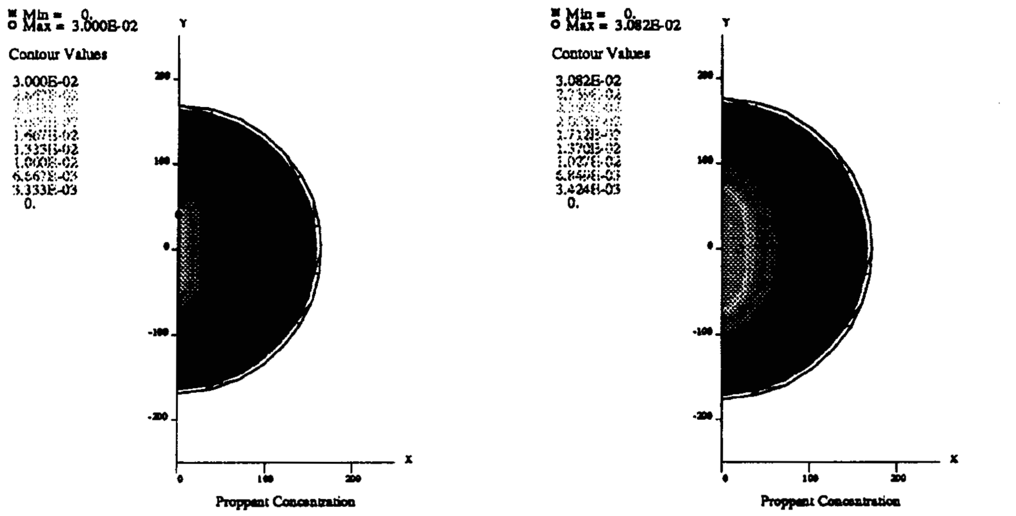

(a) after 11 Minutes of Pumping (b) after 12 Minutes of Pumping

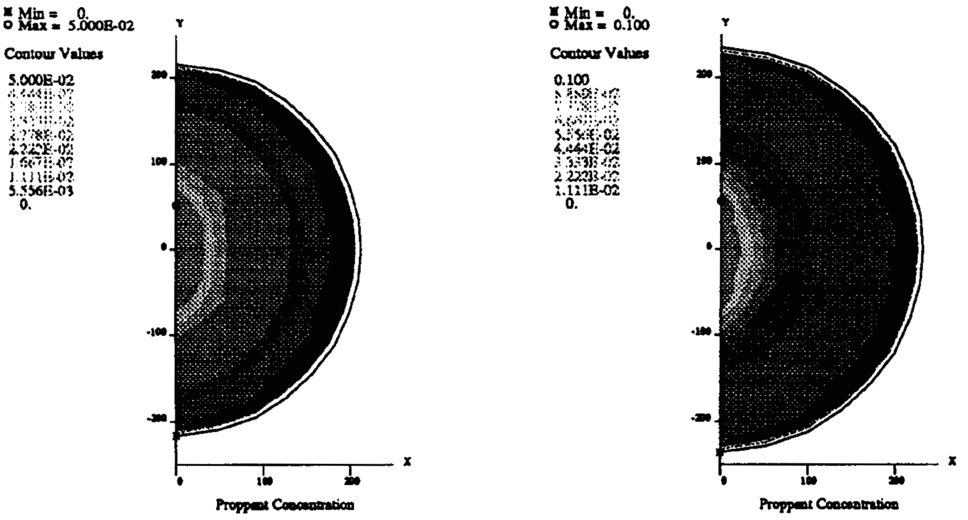

(c) after 22 Minutes of Pumping (d) after 28 Minutes of Pumping

Figure 6. Proppant concentration under uniform *in situ* stress

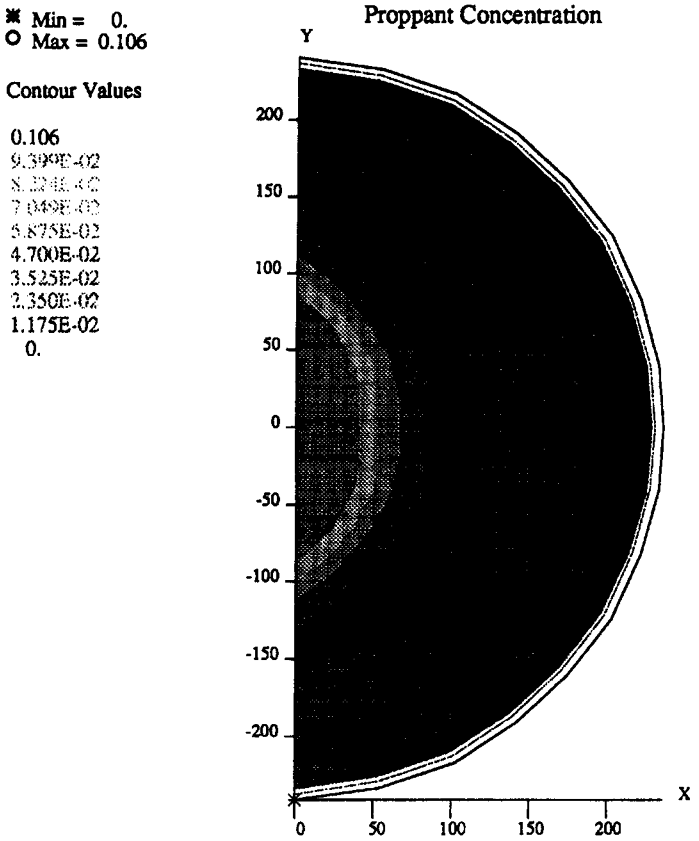

Figure 7. Final distribution of proppants (after 30 min of pumping)

6.2. 50 psi in situ stress contrast zone

Owing to this low *in situ* stress contrast, the hydraulically induced fracture is expected to be partially contained and to have the approximate shape of a triangle. In comparison with the control parameters used in the previous case (a uniform *in situ* stress), it is clear that the number of nodes to be inserted along the boundary and in the interior is increased slightly to accommodate the shape of the fracture. The final mesh is shown in Figure 8(a). A plot of the fracture front at different times is shown in Figure 8(b). It is seen that the initial elliptical fracture gradually becomes triangular owing to the *in situ* stress contrast in the region. The proppant distribution is similar to that in the circular fracture. The net borehole pressure and maximum fracture opening width are shown in Figures 8(c) and 8(d) respectively, which also show that the pressure and fracture width with proppants are higher than those without proppants. The calculated fracture shape and distribution of proppants after 11, 12, 22, 28 and 30 min of pumping are shown in Figures 9 and 10.

6.3. 400 psi in situ stress contrast zone

The hydraulically induced fracture is expected to be totally contained by the high *in situ* stress contrast. This implies that elements in the mesh will be very elongated in the direction of fracture propagation if remeshing is not applied. Therefore the grid must be properly controlled to

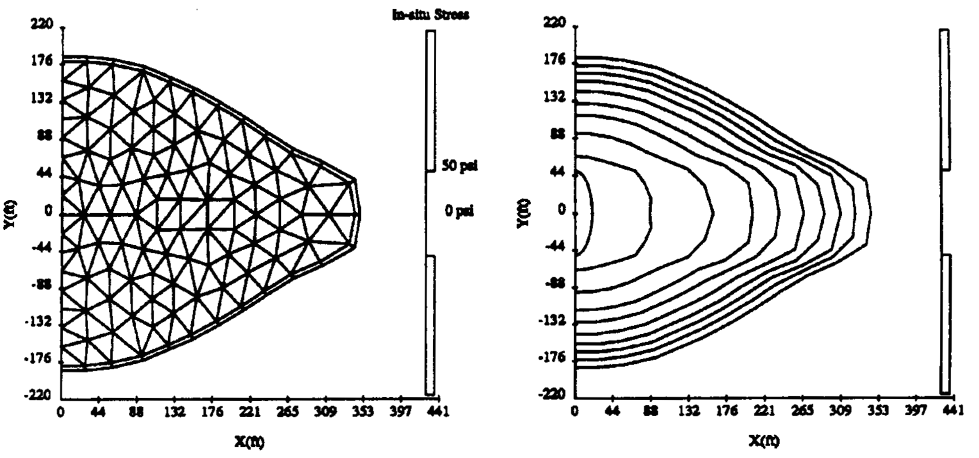

(a) Final Mesh (b) Fracture Front Contours at Different Times

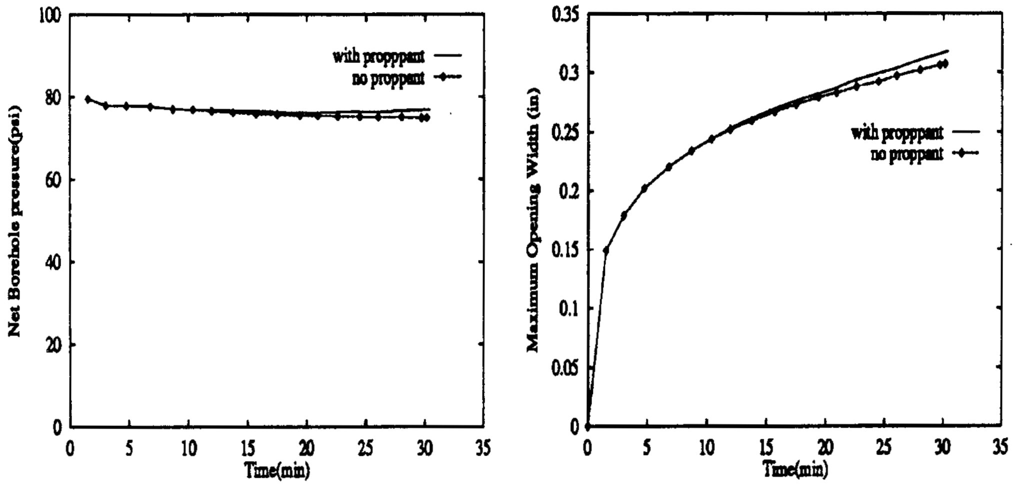

(c) Net Borehole Pressure vs Time (d) Maximum Fracture width vs Time

Figure 8. Results for *in situ* stress contrast of 50 psi

accommodate this situation. More nodes are inserted along the boundary and in the interior region to prevent excessive elongation of the elements in the domain. Since the fracture is not expected to have a significant growth in height, the number of nodes along the borehole is changed from 15 for the previous cases to nine.

The final mesh for the problem is shown in Figure 11(a). There is no excessively elongated element in the domain and the distribution of the elements is relatively uniform. The evolution of the hydraulic fracture front is shown in Figure 11(b). The hydraulic fracture is elongated and there is almost no fracture height growth in this case. The time variations in the net borehole pressure and maximum fracture opening width are plotted in Figures 11(c) and 11(d) respectively. The calculated

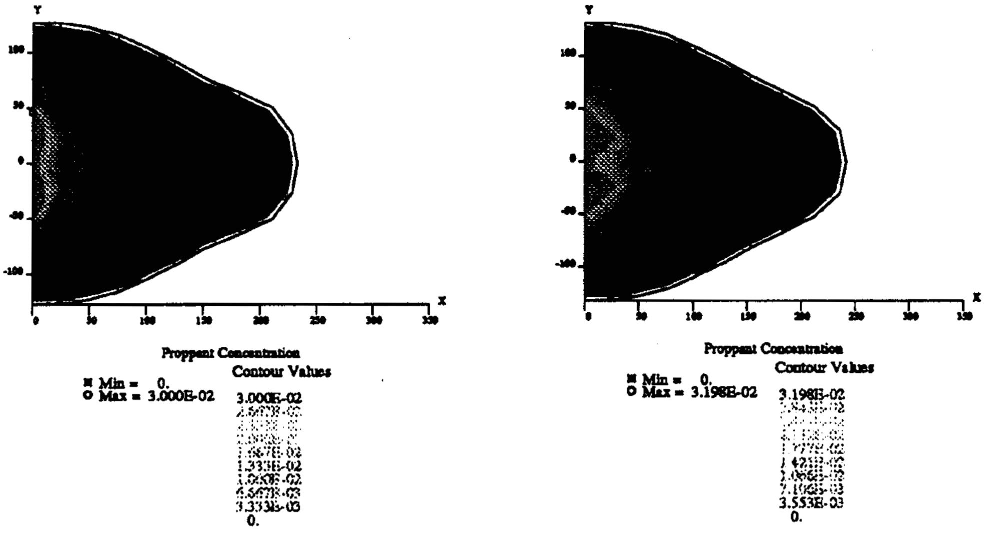

(a) after 11 Minutes of Pumping

(b) after 12 Minutes of Pumping

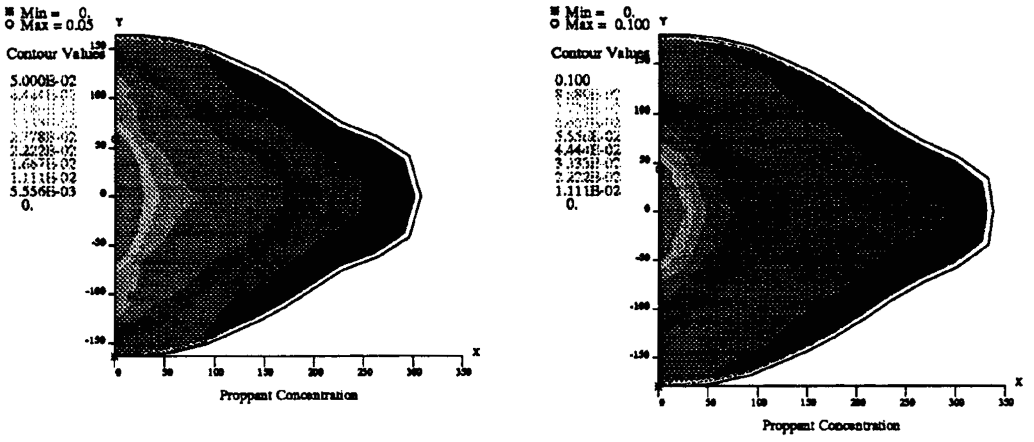

(c) after 22 Minutes of Pumping

(d) after 28 Minutes of Pumping

Figure 9. Proppant concentration under *in situ* stress contrast of 50 psi

fracture shape and distribution of proppants after 11, 12, 22 and 28 min of pumping are shown in Figure 12. After 12 min of pumping, the fracture has a total length of 350 ft and the distribution of proppant has the shape of an elongated triangle with the tip reaching to 120 ft. Note that the proppant has a higher concentration in the centre than near the boundary and finally fails to reach the boundary of the fracture, leaving a narrow no-proppant zone along the fracture contour. This phenomenon is expected, since the flow of viscous fluid is contained by the boundary and the central region has the

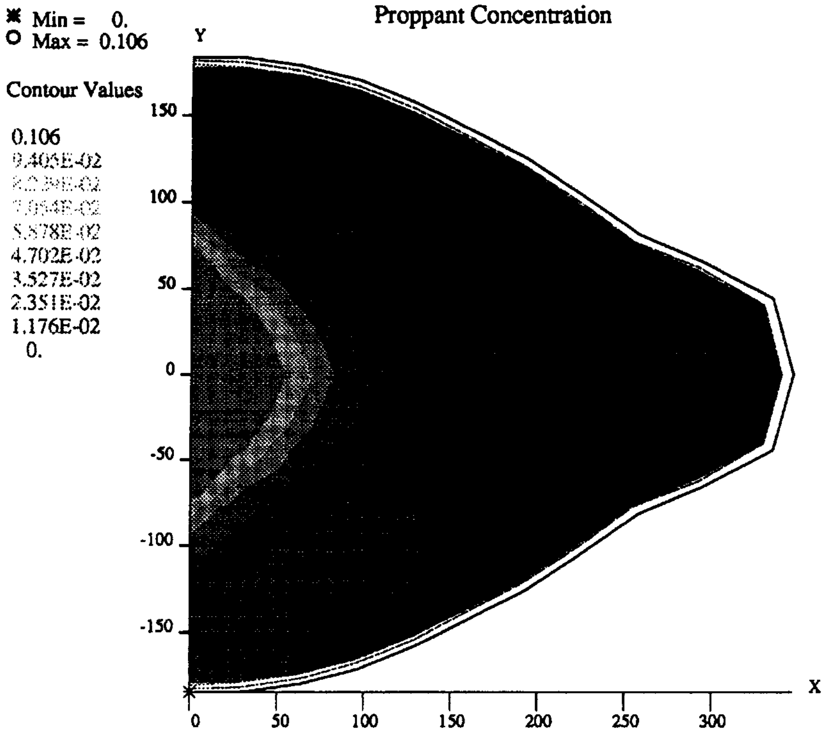

Figure 10. Final distribution of proppants (after 30 min of pumping)

highest flow velocity. The fluid velocity distribution near the boundary has a larger error than in the interior region. This causes an erratic proppant distribution in the later stages of pumping, as shown in Figure 12(d) by the wavy contour line near the boundary. If the number of elements is increased (at the expense of a very long computation time), the contours become smoother.

From the final distribution of proppant shown in Figure 12(d), we see that proppant accumulates near the fracture tip after it reaches the tip.

6.4. *A complex in situ stress distribution*

The final fracture shape and mesh under a complex *in situ* stress distribution are shown in Figure 13(a). Referring to Figure 13(b), at the beginning of the process the hydraulic fracture propagates in the 50 psi zone (for approximately 10 min), since the perforated zone is located in this zone; then the fracture breaks through the 150 psi zone and moves into the low-stress zone (designated as a reference pressure). Once the fracture reaches the low-stress zone, it has a faster propagation speed in this zone than in other zones and finally the lower fracture catches up with the upper fracture as portrayed in Figure 13(b). In this case, more nodes are inserted along the boundary and in the interior region to accommodate the complex fracture geometry. The corresponding time histories of the net borehole pressure and maximum fracture opening width are shown in Figures 13(c) and 13(d) respectively. The changes in borehole pressure and fracture opening width as the fracture breaks into the low-stress zone (at $t = 10$ min) are clearly shown in these figures. The break into the low-stress

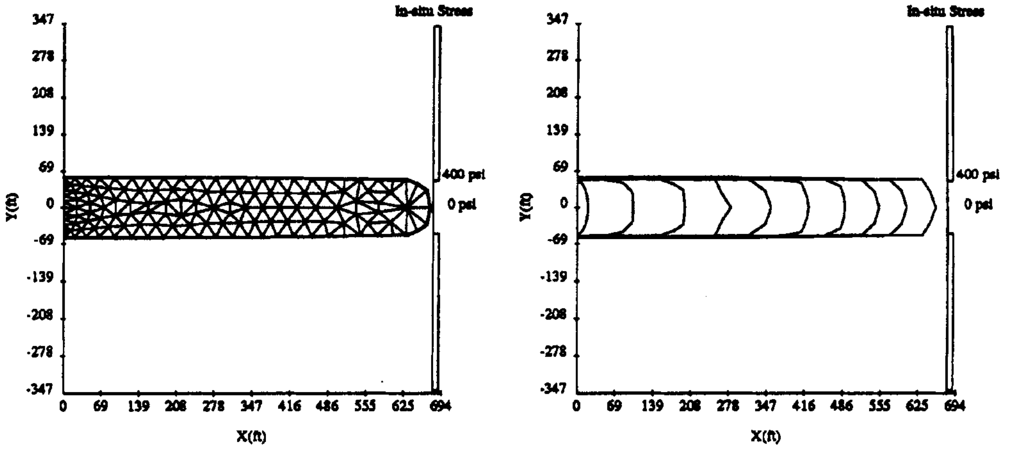

(a) Final Mesh

(b) Fracture Front Contours at Different Times

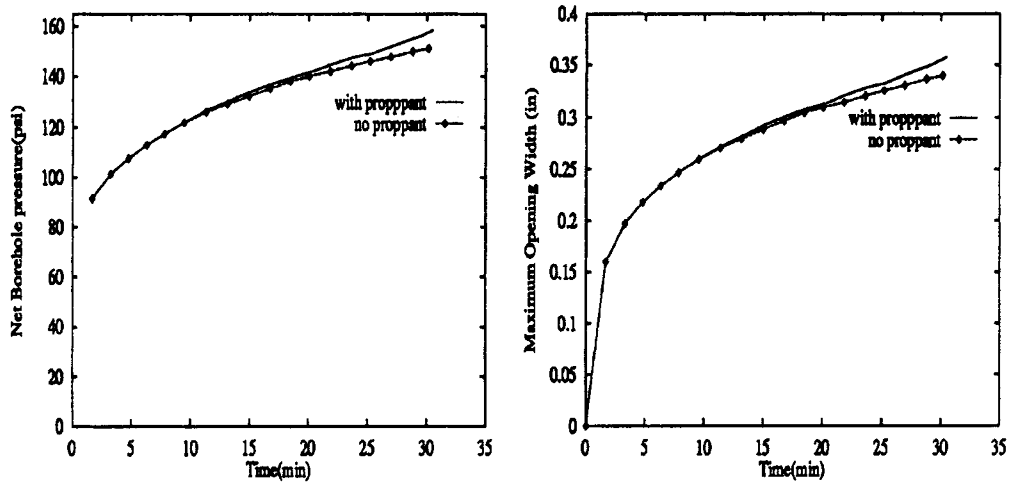

Figure 11. Results for *in situ* stress contrast of 400 psi

zone causes sudden decreases in the borehole pressure and fracture opening width, but these increase again as the fracture grows. Again the presence of proppant in the fluid causes increases in the borehole pressure and fracture opening width.

The distribution of proppants after 11, 12, 22 and 28 min of pumping is shown in Figure 14. Referring to Figure 14(b), the proppants in the lower fracture region move ahead much faster than do the proppants in the upper part.

The distribution of the fluid velocity in the fracture must be very complex at this stage of fracture propagation. It is clear that the number of elements used in this calculation is not sufficient to give a detailed description of the velocity distribution in the region. This causes the irregular proppant concentration contours shown in Figure 14(c). Nevertheless, a qualitative description of proppant distribution in the fracture is obtained.

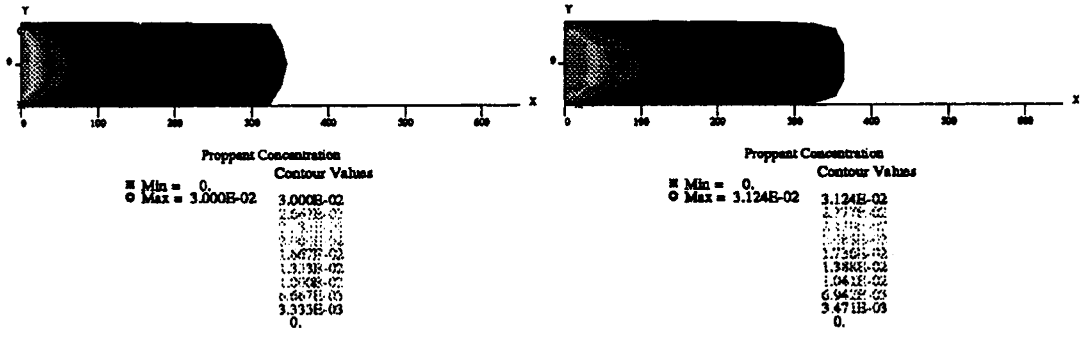

(a) after 11 Minutes of Pumping

(b) after 12 Minutes of Pumping

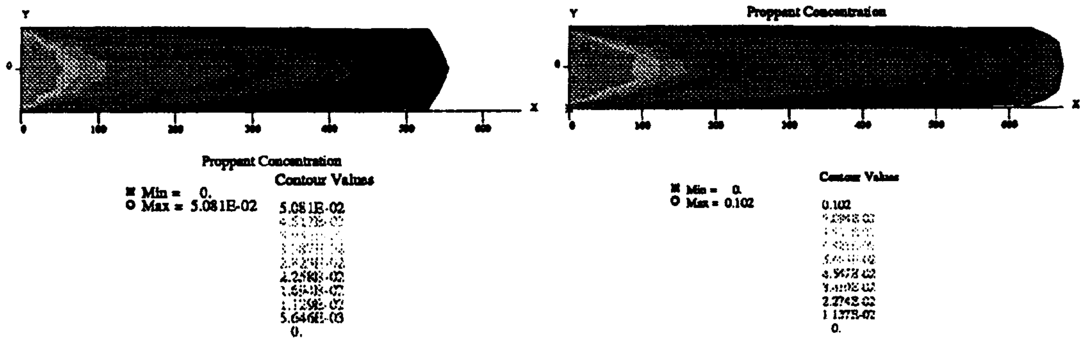

(c) after 22 Minutes of Pumping

(d) after 28 Minutes of Pumping

Figure 12. Proppant concentration under *in situ* stress contrast of 400 psi

Table IV. Timing statistics of different cases

In situ stress	Initial number of nodes	Final number of nodes	Number of time steps	Run time (min)
Uniform	63	108	80	33
50 psi	63	155	83	84
400 psi	57	192	110	120
Complex	63	245	92	161

In the later stages, as the lower fracture grows and catches up with the upper fracture, the fluid velocity in the fracture slows down and the flow pattern becomes nearly uniform. As a consequence, the proppant concentration contours become smoother and more distinguishable.

The CPU time and number of nodes in the mesh are given in Table IV for calculation on a DEC Alpha APX 3000/400.

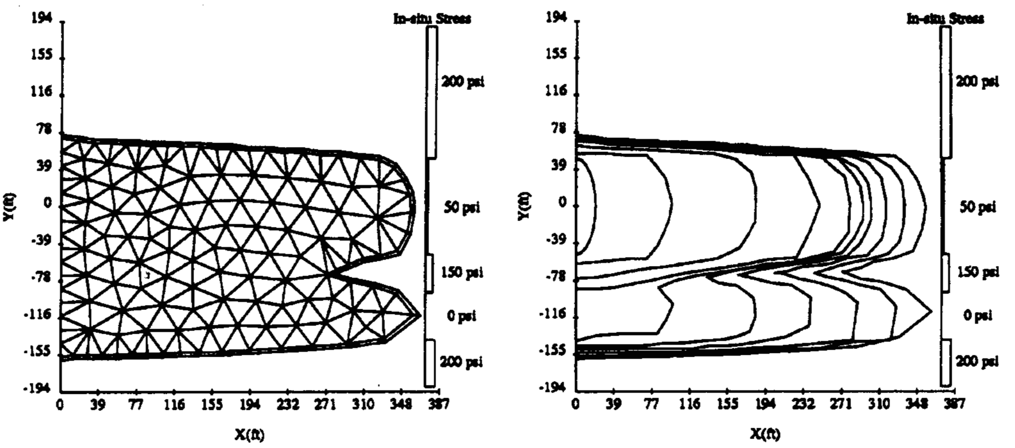

(a) Final Mesh (b) Fracture Front Contours at Different Times

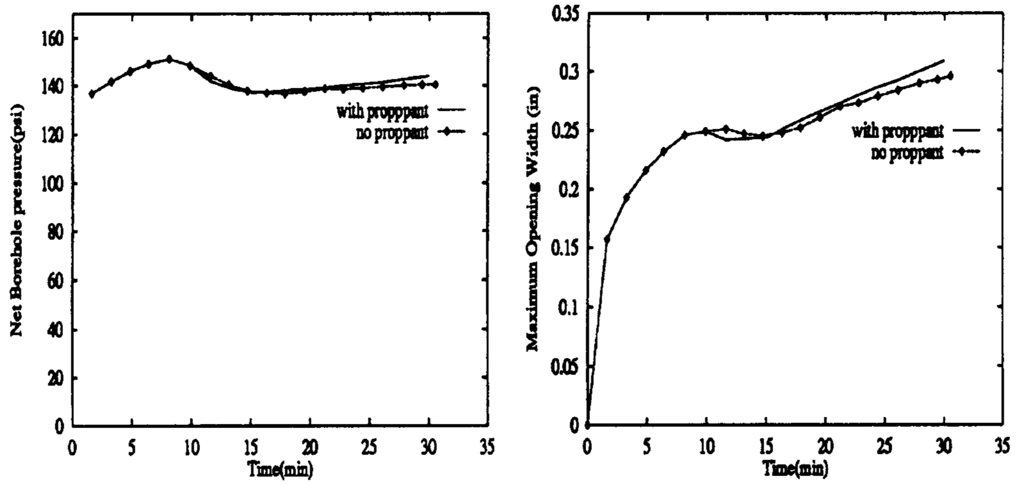

(c) Net Borehole Pressure vs Time (d) Maximum Fracture width vs Time

Figure 13. Results for complex *in situ* stress contrast

6.5. *Concluding remarks*

Based on the results from the above examples, one can conclude that the model is robust and capable of handling different cases of interest. There are few experimental data or analytical results from other 3D fracture simulators presently available for making a quantitative verification of the results from this study. Clifton and Wang[3] used a completely different slurry model in their study of proppant transport in a proprietary 3D hydraulic fracture code (Terra-frac). Since the equations used in the description of the slurry property are empirical in both studies, a correlation between the Wang–Clifton model and this model is not feasible. A comparison of fracture shape, fracture opening width and predicted net borehole pressure between this model and the Terra-frac model in the

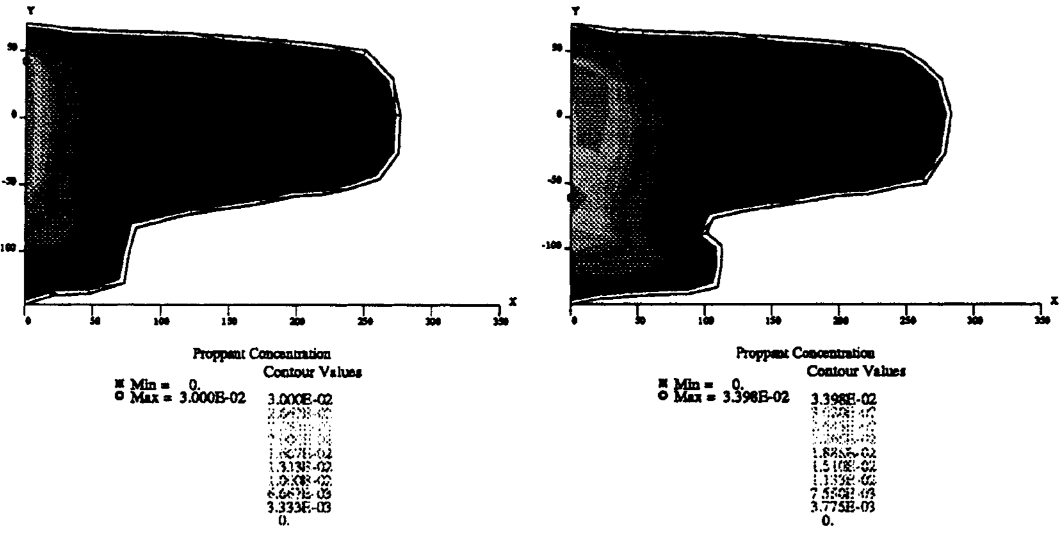

(a) after 11 Minutes of Pumping

(b) after 12 Minutes of Pumping

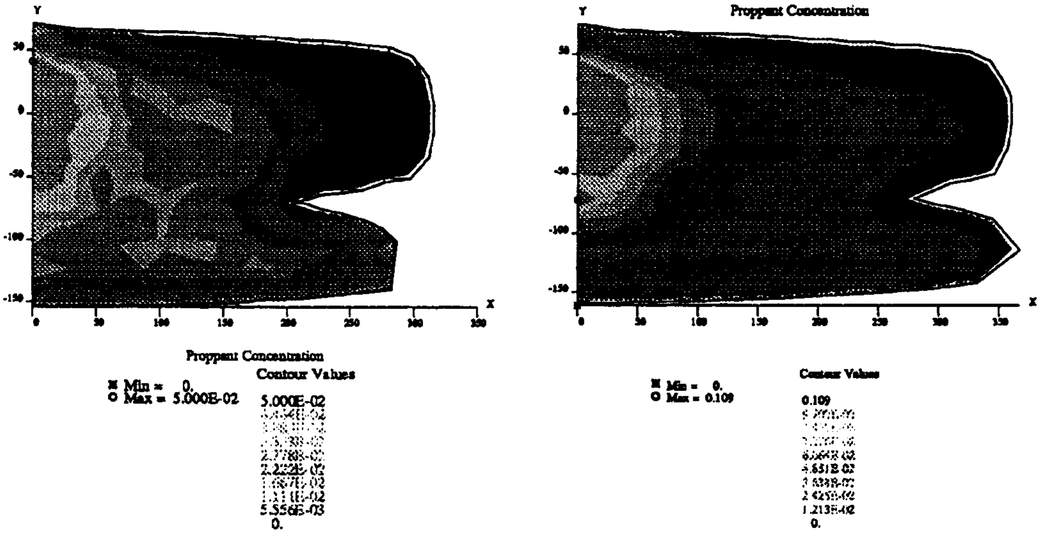

(c) after 22 Minutes of Pumping

(d) after 28 Minutes of Pumping

Figure 14. Proppant concentration under complex *in situ* stress

absence of proppant was carried out by Weng.[12] Weng demonstrated that the predictions from these models were indeed reasonably close. Therefore, if the concentration of proppant in the slurry is low (e.g. less than 20 per cent), a close agreement between the predictions from these two models can be expected.

Wang and Clifton introduce an empirical 'slip velocity' (v_s) to establish a relationship between the size of the proppant and the viscosity of the fluid. It appears that the approach taken in the present study using Shah's results is more straightforward and easier to implement. However, it is difficult at present to address the relative merit of these approaches. More basic studies on the fundamental rheological properties and on the flow of a proppant-laden slurry in a narrow channel are needed.

The present study has also clearly demonstrated that the accuracy of the solution depends on the finite element grid used in the computation and that the choice of grid for the problem depends on the distribution of *in situ* stresses. There are several subtle issues that arise regarding the coupling between the gridding problem and the fluid–fracture calculation. First, for a given fracture shape the fracture width and fluid pressure are simultaneously determined by non-linear iteration. This implies that the conservation properties are approximately satisfied in the weak Galerkin sense. However, after node insertion the current approximate solution is interpolated to the new nodes and the Delaunay triangulation will make diagonal swaps that locally change the nodal patches. This implies that locally the conservation properties will be matched to an order consistent with the finite element approximation error. In general a fine grid system is required for an accurate result but at the expense of a long computation time. Different grids could be introduced for the respective fracture and flow problems and this would substantially improve accuracy and efficiency at the cost of increased computation complexity. Other schemes such as SUPG, Taylor–Galerkin or residual bubble correction may also be introduced to treat the proppant transport more accurately and with less numerical dissipation. This is the subject of further study.

The simulation results show the effect of proppants in the fluid on the net borehole pressure and fracture width. This gives an improved understanding of the fluid–fracture process. A grid enhancement scheme is developed and incorporated in the computer program for calculating the proppant transport and fracture propagation. The enhanced grid gives not only an accurate result but also a more robust computer programme.

ACKNOWLEDGEMENT

This research was supported in part by the SLFD Industrial Associates of the University of Texas at Austin.

REFERENCES

1. R. J. Clifton and A. S. Abou-Sayed, 'On the computation of the three- dimensional geometry of hydraulic fractures', *SPE Paper 7943*, 1979.
2. R. J. Clifton and A. S. Abou-Sayed, 'A variational approach to the prediction of the three-dimensional geometry of hydraulic fractures', *SPE/DOE Paper 9879*, 1981.
3. R. J. Clifton and J.-J. Wang, 'Multiple fluids, proppant transport, and thermal effects in three-dimensional simulation of hydraulic fracturing', *SPE Paper 18198*, 1988.
4. M. R. Cleary, M. Kavvadas and K. Y. Lam, 'Development of a fully three-dimensional simulator for analysis and design of hydraulic fracturing', *SPE/DOE Paper 11631*, 1983.
5. H. Gu and C. H. Yew, 'Finite element solution of a boundary integral equation for mode I embedded three-dimensional fractures', *Int. j. numer. methods eng.*, **26**, 1525–1540 (1988).
6. G. Astarita and G. Marrucci, *Principles of Non-Newtonian Fluid Mechanics*, McGraw-Hill, London, 1974.
7. H. Gu, 'A study of propagation of hydraulically induced fractures', *Ph.D. Dissertation*, University of Texas at Austin, 1987.
8. H. D. Bui, 'An integral equations method for solving the problem of a plane crack of arbitrary shape', *J. Mech. Phys. Solids*, **25**, 29–39 (1977).

9. E. N. Mastrojannis, L. M. Keer and T. Mura, 'Growth of planar cracks induced by hydraulic fracturing', *Int. j. numer. methods eng.*, **15**, 41–54 (1980).
10. R. B. Bird, W. E. Stewart and E. N. Lightfoot, *Transport Phenomena*, Wiley, New York, 1960.
11. S. N. Shah, 'Rheological characterization of hydraulic fracturing slurries', *SPE Paper 22839*, 1991.
12. X. W. Weng, 'Incorporation of 2D fluid flow into a pseudo 3D hydraulic fracturing simulator', *SPE Paper 21849*, 1991.
13. E. N. Mastrojannis, L. M. Keer and T. Mura, 'Stress intensity factor for a plane crack under normal pressure', *Int. j. fracture*, **15**, 247–258 (1979).